International Journal of Heat and Mass Transfer 95 (2016) 426–439

Contents lists available at ScienceDirect

International Journal of Heat and Mass Transfer

journal homepage: www.elsevier.com/locate/ijhmt

Investigation on a micro-pin-fin based membrane separator

Bin An, Jinliang Xu *

The Beijing Key Laboratory of Multiphase Flow and Heat Transfer, North China Electric Power University, Beijing 102206, China

ARTICLE INFO

Article history:
Received 22 June 2015
Received in revised form 18 November 2015
Accepted 29 November 2015

Keywords:
Separator
Two-phase flow
Capillary pressure
Numerical simulation
Flow rate

ABSTRACT

We proposed a micro-pin-fin based membrane separator. An enclosed membrane with micron scale holes was symmetrically populated in a rectangular duct. When gas phase interacts with the membrane, the gas–liquid interface cannot break through the pin-fin holes due to the increased surface energy. A two-dimensional numerical model simulated the separation process. The volume of fluid (VOF) method tracked the gas–liquid interface. Multiscale grids were used. When a bubble attacks the pin-fin membrane, strong liquid circulation occurs at the membrane entrance. Pressures in the side region are larger than those in the core region. Liquid plugs are shortened due to the pressure driven flow from side region to core region to cause the bubble coalescence. The separation length was shortened while increasing the gas flow rates. The bubble lengths were weakly influenced by gas flow rates. Liquid plugs are quickly shortened following the membrane entrance. The frictional pressure drop of the two-phase mixture in the side region was larger than that of liquids in the core region, even at low gas flow rates. The ultra-large gas flow rates yielded quite large bubble pressure to exceed the capillary pressure limit, causing the separator failure. Ultra-low and large gas flow rates specified the separator operation range.

1. Introduction

Two-phase flows in microchannels have been widely investigated for electronic micro-chips, micro-reactors and micro-heat-exchangers. Microchannels have large surface to volume ratio to have large heat and mass transfer rates [1–3]. Phase separation is an important process for chemical engineering [4]. For example, the distillation and absorption contain phase separation process, which should be thoroughly investigated, especially in microscale.

Many mechanisms, including centrifugal force [5,6], gravity force [7–10] and surface tension forces [11–15], can be used to perform the phase separation. The capillary length λ is important to characterize the phase separation [3]:

$$\lambda = \sqrt{\sigma/g(\rho_l - \rho_g)} \tag{1}$$

where σ is the surface tension force and $\rho_l - \rho_g$ is the density difference between liquid and gas phases. When the structure size is reduced to below λ, the capillary effect becomes important.

The phase separation in microsystems was reviewed by Wiesegger et al. [16]. Gupta et al. [17] commented on the non-dimensional parameters involved in two-phase system such as Reynolds number ($Re = \rho uD/\mu$): the inertia relative to viscous force; the Froude number ($Fr = \rho u^2/\Delta\rho gD$): the inertia relative to gravity; the Bond number ($Bo = \Delta\rho D^2 g/\sigma$): the gravity relative to surface tension force; the capillary number ($Ca = \mu u/\sigma$): the viscous force relative to surface tension force; and the Weber number ($We = \rho u^2 d/\sigma$): the inertia relative to the surface tension force. These dimensionless parameters indicated that as the channel size decreases, the surface tension force becomes more important.

The phase separation in capillaries or in a capillary network has been investigated by various researches [18–25]. Membranes were used to deal with the phase separation. The gas–liquid interface was stabilized with a membrane during the evaporation process [12]. Different membranes were investigated on the separation factor and the distillate flux rate. Only the feed concentration influenced the separation efficiency. David et al. [12] used a hydrophobic *PTEE* membrane with 220 nm pores to vent the vapor phase from water boiling in microchannels.

Kraus and Krewer [13] used a membrane combining hydrophilic and hydrophobic materials to separate CO_2 from water/methanol mixtures in microchannels for direct methanol fuel cells. Effects of the temperature, humidity, flow rates and orientation on the separation efficiency were considered. The separation efficiencies could reach 100%. Zenith et al. [26] used the interface tracking method (volume of fluid, called VOF) in Fluent to model the phase separation in a separator that was experimentally studied by Kraus and Krewer [13]. The separator orientation with

* Corresponding author. Tel.: +86 (10)61772613.
E-mail address: xjl@ncepu.edu.cn (J. Xu).

http://dx.doi.org/10.1016/j.ijheatmasstransfer.2015.11.096
0017-9310/

Nomenclature

a	core region width (μm)
A_{pore}	pore cross sectional area (m^2)
Bo	Bond number
b	width of each side region (μm)
Ca	capillary number
C_d	discharge coefficient
Co	courant number
d	gap between micro-pin-fins (μm)
D	bare duct width (μm)
E	surface energy (J)
Eo	the ratio between gravity and surface tension forces
F_{vol}	interface-induced volume force vector (N)
Fr	froude number
f	bubble appearance frequency (s^{-1})
g	gravitational acceleration (m s^{-1})
H	bare channel height (μm)
J	superficial velocity (m s^{-1})
K	the work which pushes the gas bubble moving (J)
L	channel length (mm)
L_s	the slug bubble length (μm)
n_g	the number of pores that are occupied by gas in the side region
n_l	the number of pores that are occupied by liquid in both sides
$\hat{n}_w$	the unit vector normal to the wall
P	pressure (Pa)
Q	volume flow rate (m^3 s^{-1})
Re	Reynolds number
s_1, s_2	moving distance from state A to state B (m)
t	time (ms)
$\hat{t}_w$	the unit vector tangent to the wall
T	the time period of Bubble appearance (ms)
u	velocity in x coordinate (m s^{-1})
u_{in}	inlet velocity (m s^{-1})
V	bubble volume (μm^3)
V_r	radial velocity (m/s)
v	velocity in y coordinate (m s^{-1})
$\vec{v}$	velocity vector
w	micro-pin-fin width (μm)
We	Weber number
x	x coordinate
y	y coordinate
z	z coordinate

Greek letters

α	void fraction
β_L	the ratio of a slug bubble length related to a bubble unit length
δ	film thickness (μm)
φ	two-phase multiplier
κ	interface curvature (m^{-1})
μ	dynamic viscosity (Pa s)
θ	contact angle
ρ	density (kg m^{-3})
σ	surface tension (N m^{-1})
λ	Laplace-length (m)

Subscripts

B	bare duct section
b	bubble
$core$	core region
g	liquid phase
in	inlet
l	vapor phase
lo	the whole two-phase flow rate flowing as liquid only
M	modulated flow section
$side$	side region
w	wall

respect to gravity was found to have small influence on the separator performance.

We proposed a phase separator in Xu et al. [27]. The separator was formed by populating an enclosed micro-membrane in the microchannel center. When a bubble train in the bare duct interacted with the micro-membrane, a single bubble was separated into two daughter bubbles to flow in the two side regions. The separated bubbles did not enter the micro-membrane inside due to the increased surfaced energy (see Fig. 1). A multiscale numerical scheme using the volume of fluid (VOF) method tracked the gas–liquid interface. The results identified that the separator consisted of a phase separating section and a fully phase separation section. Here the phase separating section refers to the bubble merging in the side region and the liquid plugs are gradually shortened along the flow direction. The fully phase separation section refers to that the bubbles are completely merged. Within the separating section, the two side regions contained confined bubble train. The liquid plugs were gradually shortened along the flow direction, caused by liquid flowing towards the micro-membrane inside. Liquid circulations were observed within liquid plugs. The gas–liquid could be fully separated.

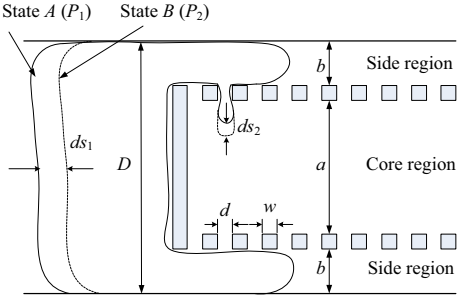

Fig. 1. The drawing to show the mechanism why bubble cannot enter micro-membrane inside.

The present work continued our previous work. Regarding the proposed micro-separator using the micro-membrane structure, the question may arise that what are the minimal and maximum flow rates that are adapted to a given micro-separator design. In order to answer this question, we fixed the liquid flow rate, but gas flow rates are continuously varied from minimum to maximum at which gas bubble begins to break-through the micro-membrane. The flow field and bubble dynamics were carefully examined during the separation process when the flow rates are changed. It is found that the micro-separator can operate at very low gas flow rate. The maximum gas flow rate corresponds to the dynamic pressure exceeding the maximum capillary pressure that can be provided by the membrane pore.

2. The background

Fig. 1 shows the separator with micro-membrane in a rectangular duct. Because the computation resource is huge for a three-dimensional problem with many micro-pores involved, the

problem was simplified as a two-dimensional one, inferring infinite size perpendicular to the paper plane. The micro-pin-fins were lined to form an enclosed micro-membrane with an open exit. Because the front plane of the enclosed membrane directly receives the fluid stream from its upstream, the front plane is solid without holes to prevent gas phase from entering the membrane inside (see Fig. 1). The duct cross section was divided into a core region and two side regions close to the side duct walls. The gap between two neighboring pin-fins was d (recorded as the pore diameter). Each of the two side regions had the width of b. The core region had the width of a. The pin-fin had square cross section with a width of w (see Fig. 1). The depth perpendicular to the paper plane is infinite but it is assumed a limited value of H.

Bubbles are difficult to enter the core region if d is sufficiently small. This is because the surface energy of gas bubble should be increased when the bubble interface moves from a larger space to a smaller space [28]. Considering a large bubble with its width identical to the duct width D is penetrating the pore with its size d, the surface energy of the gas bubble between state A (initial state) and B (ending state) is

$$dE = 2\sigma(d+H)ds_2 - 2\sigma(D+H)ds_1 \tag{2}$$

where E is the surface energy, σ is the surface tension, d is the gap of the micro-pin-fins, D and H are the channel width and depth, respectively, ds_1 is the moving distance from state A to state B in the bare duct, ds_2 is the distance penetrating the micro-pore (see Fig. 1). The mass conservation for the gas bubble yields

$$dHds_2 = DHds_1 \tag{3}$$

Thus the work required to transform the gas bubble from state A to B is

$$dK = P_1 DHds_1 - P_2 dHds_2 \tag{4}$$

where K is the work, P_1 and P_2 are the gas bubble pressures at the state A and B, respectively. The P_1 and P_2 had the following relationship with $dK = dE$.

$$P_1 - P_2 = 2\sigma\left(\frac{1}{d} - \frac{1}{D}\right) \tag{5}$$

The second term of the right side of Eq. (5) contributes less to the pressure difference due to $D \gg d$. Giving $\sigma = 0.07275$ N/m for an air–water system at 20 °C and $d = 5$ μm, $P_1 - P_2 = 29$ kPa, indicating a pressure difference of about 30 kPa required to penetrate a bubble interface within the micro-pores. It is noted that Eq. (5) is deuced using the surface energy equation (Eq. (2)) and the mass conservation equation (Eq. (3)). Eq. (5) is not related to the solid surface wettability. Thus, the contact angle term does not appear in Eq. (5).

It should be noted that the air–water system is widely used for thermal and chemical engineering applications. Thus, the air–water system is used in this study. In Eq. (5), D is the channel width, and d is the gap between two neighboring pin-fins (see Fig. 1).

3. Configuration and problem statement

Fig. 2 shows the microfluidic with infinite z coordinate. The separator consisted of a bare duct part and a separating flow part. The flow field and bubble interface can be compared between the bare duct part and the separating flow part. An enclosed micro-membrane with an open exit was located symmetrically in the rectangular duct. The open exit was used to discharge fluids. The micro-membrane was formed by micro-pin-fin structure. For practical applications, the two open exits for both liquid and gas phases are connected with capillary tubes for fluid transport. The equal

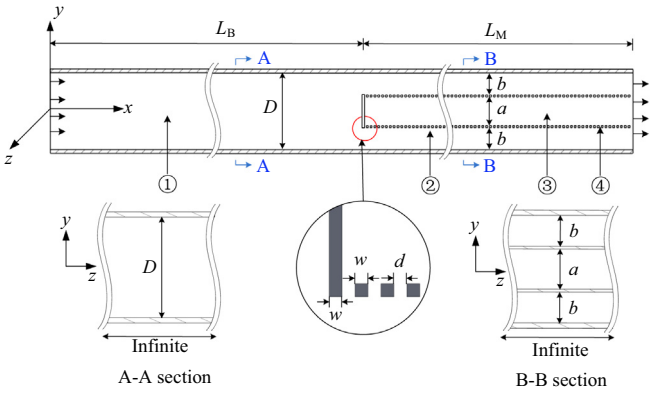

Fig. 2. The two-phase separator (two-dimensional geometry with infinite z coordinate).

pressures at the exit plane of gas and liquid phases can be realized by adjusting the exit capillary tube sizes.

The bare duct width and depth were D and H, respectively. The two parts had the length of L_B and L_M, respectively. The micro-pin-fin had the square cross section with the width of w. The gap between two neighboring pin-fins was d. The two side regions had the gap width of b and the core region had the width of a. The major dimensions are $D = 400$ μm, $a = 235$ μm, $b = 77.5$ μm, $w = 5$ μm and $d = 5$ μm. The three-dimensional coordinates of x, y and z were marked in Fig. 2. The regions 1, 2, 3 and 4 referred to bare duct, side region, core region and membrane structure with pin fin structure. The working principle of the separator was described in Fig. 1, together with Eqs. (2)–(5). The problem of the micro-separator is difficult because the separation mechanism is unknown and there are no correlations about the separation efficiency and separation length.

Fig. 3 shows the half computation domain due to the symmetrical device. The problem fixed the inlet fluid velocity u_{in} at $x = 0$. In order to give the flow rates of gas and liquid phases, Taylor bubbles were assumed to populate at $x = 200$ μm consecutively at the time period of $T = 1/f$, where f is the bubble appearance frequency. The Taylor bubble contained a body (360 μm in y direction and infinite in z direction) and a half circle (180 μm in radius). The total bubble length was 540 μm. Based on Qian and Lawal [29], the bubble length is influenced by the channel geometry shape and size, as well as the flow rates of the two-phases. At specific flow rates of liquid and gas phases, the bubble lengths have a statistical distribution. The bubble length here was selected as the size that had maximum distribution at the specific flow rates in a rectangular microchannel. With this information a single bubble had the volume of $V_b = 1.81 \times 10^{-7}$ m^3. The two-phases had the flow rates of $Q_g = V_b f$ and $Q_l = u_{in}D - Q_g$. The flow rates were characterized in terms of per unit depth in z direction. The superficial velocities of the two-phases are $J_g = Q_g/D$ and $J_l = Q_l/D$. The Reynolds numbers were defined based on the superficial velocities of the two-phases:

$$Re_l = \frac{\rho_l J_l D}{\mu_l}, \quad Re_g = \frac{\rho_g J_g D}{\mu_g} \tag{6}$$

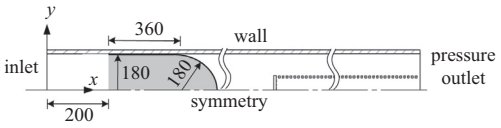

Fig. 3. Computation domain and boundary conditions (all dimensions are in μm).

where the subscripts g and l represent gas phase and liquid phase, respectively.

4. Numerical method and solution procedure

4.1. Governing equations

The interface can be explicitly captured if the interface is apparently larger than the grid size [30]. Only a single set of conservation equations are solved and the interface is tracked using an additional advection equation. The bulk properties of the fluid are the volume fraction weighted average of the properties of the two fluids. An additional equation for the gas void fraction is solved to identify the interface location. The governing equations in terms of volume-of-fluid (called VOF) are:

The advection equation of the volume fraction:

$$\frac{\partial \alpha}{\partial t} + \vec{v} \cdot \nabla \alpha = 0 \tag{7}$$

The continuity equation:

$$\nabla \cdot \vec{v} = 0 \tag{8}$$

The momentum equation:

$$\frac{\partial}{\partial t}(\rho \vec{v}) + \nabla \cdot (\rho \vec{v} \vec{v}) = -\nabla P + \nabla \cdot \left[\mu(\nabla \vec{v} + \nabla \vec{v}^T)\right] + \vec{F_{vol}} \tag{9}$$

in which

$$\rho = \rho_l \alpha_l + \rho_g \alpha_g \tag{10}$$

$$\mu = \mu_l \alpha_l + \mu_g \alpha_g \tag{11}$$

The ratio between gravity and surface tension forces is defined as:

$$Eo = \frac{g \Delta \rho D^2}{\sigma} \tag{12}$$

where g is the gravitational acceleration, $\Delta\rho$ is the density difference of the liquid and gas. Bretherton [31] used Bond number, $Bo = Eo/4$. Both Eo and Bo are significantly smaller than 1, thus the gravity force is not considered in this study. In Eqs. (7)–(9), α is the void fraction, t is the time, $\vec{v}$ is the velocity vector, ρ and μ are the density and viscosity, respectively. The volume force due to the surface tension effect in Eq. (9) was modeled as [32]

$$F_{vol} = \sigma \frac{\alpha_l \rho_l \kappa_l \nabla \alpha_l + \alpha_g \rho_g \kappa_g \nabla \alpha_g}{0.5(\rho_l + \rho_g)} \tag{13}$$

where κ is the interface curvature having the following expression:

$$\kappa_l = -\kappa_g = -\nabla \cdot \left(\frac{\nabla \alpha_l}{|\nabla \alpha_l|}\right) \tag{14}$$

The contact angle of the fluid contacted with the wall adjusts the surface normal in cells near the wall, resulting in the curvature adjustment of the surface near the wall. If the contact angle is recorded as θ, the surface normal at the live cell next to the wall is:

$$\hat{n} = \hat{n}_w \cos\theta + \hat{t}_w \sin\theta \tag{15}$$

where $\hat{n}_w$ and $\hat{t}_w$ are the unit vectors normal and tangent to the wall, respectively. The contact angle is only important when both of the phases contact with the solid wall or the liquid film around the gas bubble is so thin that the van der Waal forces act across the film. Once a slug bubble is formed with a liquid film on the wall, wall adhesion plays no role to decide the bubble shape. This treatment is similar to that of Mehdizadeh et al. [33]. The liquid film thicknesses were paid attention here. Because the bubble is not too long, the liquid film thicknesses are varied along the bubble body length. We captured the thinnest liquid film thickness to be 13.6 μm in the bare tube section. Alternatively, such liquid film thicknesses are predicted by the expressions such as $\delta/D = 0.25Ca^{0.5}$, $\delta/D = 0.67Ca^{0.667}$, and

$$\frac{\delta}{D} = \frac{0.67Ca^{2/3}}{1 + 2.5(1.34Ca^{2/3})} \tag{16}$$

in Refs. [31,34,35]. The liquid film thicknesses are computed based on the above expressions are 12.4 μm, 16.5 μm and 13.7 μm, respectively. The present simulated value of 13.6 μm is very close to those predicted by the expressions in Refs. [31,34,35]. It is noted that the liquid film thickness was further thinner in the modulated flow section with pin-fin structure.

4.2. Grid generation and interface tracking

Fig. 4 shows the two-dimensional grid generation system. The grids are created to have multiscale behavior. Special attention was paid to the near wall region and the near micro-pin-fin region. Regarding the near wall region, very fine grids are used with δ_1 = 5 nm for the first layer on the wall (see Fig. 4). The second layer had the grids of $\delta_2\delta_1$ = 1.2. The grids gradually become coarse with the adaption factor of 1.2. The fine sub-layers on the wall had the total thickness of 30 μm. The criterion is that the sub-layer thickness should be significantly larger than the liquid film thickness. In this study, the sub-layer of 30 μm is more than two times of the liquid film thickness when the bubble is flushing the channel wall. The grids far away from the wall and the micro-pin-fin region had the size of 3.125 μm. Much fine grids are used near the pin-fin pores. There are 8 grids within a single hole between two neighboring pin fins. The grids become coarse away from the micro-pin-fins based on the adaptor factor of 5:1. The sensitivity analysis of the grid number on the flow was performed. It was found that further refinement of grids had no influence on the flow behavior.

It is known that the computation results are relied on the grid numbers. Fig. 4 shows the grid construction with the grid number of 79,089. However, the cases of grid number of 54,574 and 148,444 are also tried. The parameters of bubble dynamics such as liquid film thickness, bubble velocities and stabilized bubble lengths are compared among the cases with the three grid numbers. It is found that the computation results are not changed anymore when the grid number is up to 79,089. Thus, the results presented in this paper are reliable.

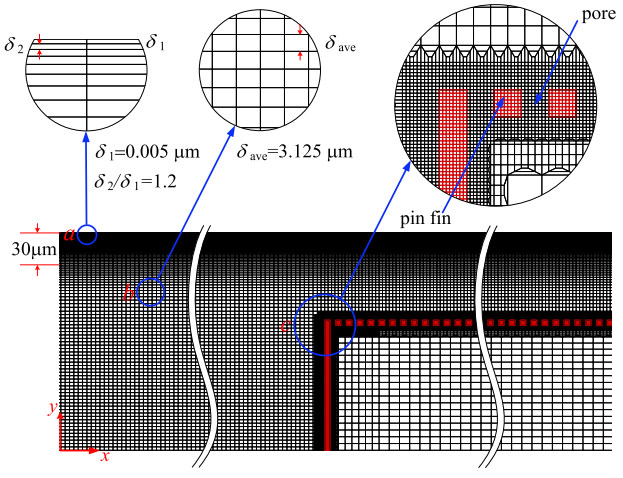

Fig. 4. Grid generation and enlarged grids near the duct wall and pin-fin area.

4.3. Differencing schemes

The finite volume method (FLUENT version 6.3.26) solved Eqs. (7)–(9) and boundary conditions. The second order upwind scheme was applied for momentum discretization and the SIMPLE algorithm dealt with the pressure–velocity coupling. The geometric reconstruction scheme captured the interfaces accurately. The time marching of the continuity and momentum equations was fulfilled by the first-order implicit scheme. The time step is controlled by the Courant number, written as

$$Co = \frac{\Delta t}{\Delta x/u} \tag{17}$$

where Δx is the grid size and u is the fluid velocity. The Courant number was set to 0.25 in this study.

5. Results and discussion

5.1. Verification of the numerical simulation and runs of this study

In order to verify the correctness of the present numerical simulation, we calculated the pressure drop in a two-dimensional channel without micro-membrane insert. The channel duct width was 400 μm in y direction and the z coordinate is infinite. The duct length was 16.0 mm. The two-phase flow rates were $Q_l = 2.67 \times 10^{-4}$ m^3/s and $Q_g/Q_l = 4/6$. The bubble generation frequency was about 1000 Hz, corresponding to the bubble appearance time period of about 1 ms (see the basic run in Table 1). Because Taylor bubbles were orderly populated along the flow direction, the pressure drop was evaluated in terms of a Taylor bubble unit. The pressure drop gradient was calculated as 0.284 MPa/m. On the other hand, Kreutzer [36] gave the pressure drop gradient as

$$-\left(\frac{dP}{dz}\right)_s = \beta_L \frac{2\mu_L(J_l + J_g)}{D^2} \times 16\left(1 + 0.07\frac{D}{L_s}\left(\frac{Re}{Ca}\right)^{0.33}\right) \tag{18}$$

where μ_l is the liquid viscosity, J_g and J_l are the superficial velocities of gas and liquid, respectively, Re and Ca are the Reynolds number and capillary number, assuming the whole mixture flowing as liquid only, β_L is the ratio of a slug bubble length related to a bubble unit length, it is 0.54 for the present case. L_s is the slug bubble length, equals to 0.66 mm. The pressure drop gradient by Eq. (18) was 0.271 MPa/m, deviating from our simulated value by less than 5%, indicating the correctness of our numerical simulation.

The liquid volume flow rate was fixed as 2.67×10^{-4} m^3/s per unit depth in z direction. However, the inlet velocity u_{in} is increased gradually, from S-2 to L-2. The S-2 run had the smallest gas flow rate for which $Q_g/Q_l = 2/6$. Such run was to explain the phase separation mechanism at low gas flow rate. The basic run had $Q_g/Q_l = 4/6$, which was determined assuming the equal average velocities of gas flowing in the two side regions and liquid flowing in the core region. The L-1 and L-2 runs had larger gas flow rates. We will show that L-1 was a run for normal phase separation. L-2 had the largest gas flow rate, for which bubbles had large pressure to penetrate holes between neighboring pin fins. Bubble breakup happened thus the device does not work, practically.

In order to further verify the correctness of the present computations, pressure gradients in the bare tube section were listed in the last two columns of Tab.1. It is seen that the simulated pressure gradients are well agreement with the predictions by Eq. (18), for all of the five runs encountered in this paper.

5.2. Phase separation process

This section describes the phase separation process for the basic run (see Table 1). Fig. 5 tracked the bubble locations when the bubble was traveling from the bare duct to the phase separator. The initial time ($t = 0$) was defined when the bubble appeared at the location shown in Fig. 3. Fig. 5a and b shows the bubble in the bare duct. The Taylor bubble was 660 μm in length, and the liquid plug between two neighboring Taylor bubbles had a length of 562 μm. The Taylor bubble consisted of a bubble nose, a bubble body and a bubble tail. The liquid film was formed between the Taylor bubble body and the duct wall. The shape of the bubble tail was dependent on the capillary number and it was protruding due to the small capillary number for the air–water system. This shape was consistent well with the analysis reported by Taha and Cui [37]. The flow field at the center between two neighboring bubbles exhibits perfect parabola distribution across the duct width. The parabola distribution was slightly deformed when the axial location approaches the bubble nose or bubble tail.

Fig. 5c and d shows the bubble interacting with the micro-membrane. Liquid inside the micro-membrane was almost stationary. The bubble was separating into two daughter bubbles, but only one bubble was shown due to the half computation domain demonstration. The bubble did not enter the core region. The distance between two neighboring micro-pin-fins, d, was small enough so that the surface energy increment for the bubble penetrating into small holes was larger than the pressure difference across the two sides of the micro-membrane. The apparent change of the liquid film thickness was observed.

Fig. 5e and f shows the two daughter bubbles completely formed in the two side regions of the separator. The daughter bubbles had thin liquid films for most part of its length. But thick liquid film was observed at the daughter bubble tail.

Fig. 5g shows two bubbles in the side regions, which were merging together. The liquid velocity field inside the core region was successfully established. The liquid films on the side walls are ultra-thin, which was about 4 μm. The liquid in the core region also exhibits the parabola velocity distribution across the channel width. Fig. 5h shows the complete coalescence of neighboring bubbles in the side regions. The co-current flow was established in both the side regions and the core region.

An alternative way to present the flow field uses the reference coordinate, which was attached on the Taylor bubble body (see Fig. 6). Because the flow field was plotted assuming the "stationary" Taylor bubble, the flow field was significantly different from that shown in Fig. 5. The circulating flow in liquids was apparently observed in the bare duct section (Fig. 6a–c) and at the

Table 1
Runs in this study.

Run	u_{in} (m/s)	Q_{total} (m^3/s)	Q_g/Q_l	Q_g (m^3/s)	Q_l (m^3/s)	$1/f$ (s)	dp/dz (MPa/m) simulation	dp/dz (MPa/m) correlation
S-2	0.89	3.57×10^{-4}	2/6	8.93×10^{-5}		2.02×10^{-3}	0.118	0.129
S-1	1.00	4.02×10^{-4}	3/6	1.34×10^{-4}		1.35×10^{-3}	0.191	0.194
Basic	1.12	4.46×10^{-4}	4/6	1.79×10^{-4}	2.67×10^{-4}	1.01×10^{-3}	0.271	0.284
L-1	1.23	4.92×10^{-4}	5/6	2.24×10^{-4}		8.09×10^{-4}	0.305	0.319
L-2	1.34	5.36×10^{-4}	6/6	2.69×10^{-4}		6.74×10^{-4}	0.375	0.380

Note: volume flow rates are defined based on per unit length in z direction.

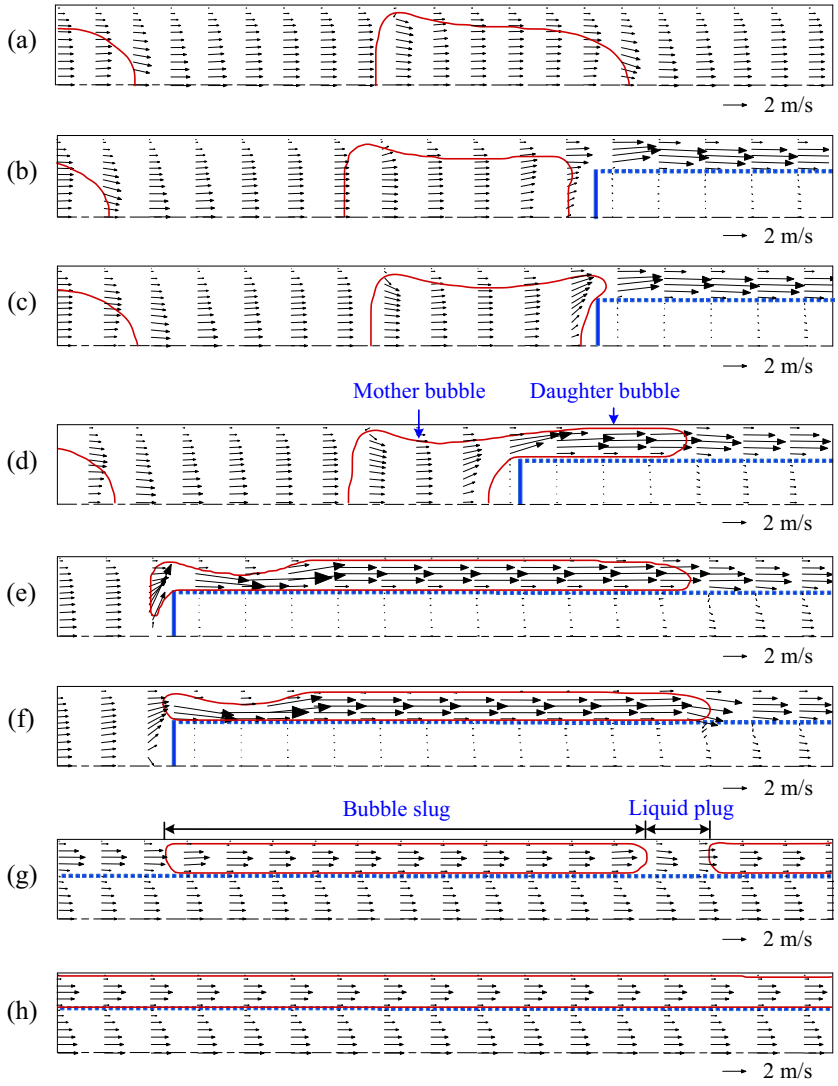

Fig. 5. Bubble shape and velocity field for basic run (see Table 1): (a) t = 14.71 ms, x = 3.9–5.9 mm; (b) t = 16.84 ms, x = 6.6–8.6 mm; (c) t = 16.89 ms, x = 6.6–8.6 mm; (d) t = 17.04 ms, x = 6.8–8.8 mm; (e) t = 17.32 ms, x = 7.7–9.7 mm; (f) t = 17.34 ms, x = 7.7–9.7 mm; (g) t = 18.33 ms, x = 9.9–11.9 mm; (h) t = 21.02 ms, x = 13.4–15.4 mm.

micro-membrane entrance (Fig. 6b–d). Because the velocities were defined as the "real" velocity subtracting the Taylor bubble velocity, and liquids are almost stationary when one stands on the earth coordinate, the core region entrance had apparent negative velocities and flow streams are parallel. When the daughter bubbles are fully separated from the mother bubble, negative velocities are observed downstream of the daughter bubble in the two side regions (see 6e–g). This indicates that liquid plugs between two neighboring bubbles in the side region had smaller velocities than the bubbles, explaining the coalescence of neighboring bubbles, which is the main reason to cause the full separation of the gas and liquid phases. Fig. 6h shows the time on which the two-phases are fully separated. Velocities within the bubble had parabola distribution. But in the core region, velocities are negative near the pin-fin membrane and positive near the core region center. Later we will show that velocities in the core region strongly depend on the flow rate ratios between the gas and liquid phases.

The pressure distribution was examined over the half computation domain at various bubble locations (see Fig. 7). Referenced pressure related to the environmental pressure was used and different pressure scales are used in Fig. 7. Pressures in the bare duct section are apparently larger than those in the separating section, due to the fact that population of micro-pin-fin membrane in the duct increases the two-phase drops. Pressures inside bubbles are larger than those outside of the bubble, caused by the pressure difference across the gas–liquid interface balanced by the capillary pressure related to the surface tension force and the interface curvature. Pressures inside the bubble in the side region are quite uniform because the long bubble had quite small interface curvature, except at the bubble front and tail locations. Always, the gas phase in the side region had larger pressures than in the core region.

Fig. 8 plotted the radial velocities across the pin-fin membrane. Positive radial velocity means the flow towards the side region. Alternatively, negative radial velocity indicates the flow from the side region to the core region. Four bubbles are focused. The first bubble is attacking the micro-pin-fin membrane. The second, third and forth daughter bubbles are gradually shortening the liquid plug lengths along the flow direction, indicating the coalescence process in the side region. It is observed that within the liquid plug between two neighboring daughter bubbles in the side region, mass transfer from the side region to the core region happened, except at the bubble tail, explaining the coalescence mechanism of the bubbles in the side region. Local flow fields were examined near the second bubble front (point A), the third bubble tail (point

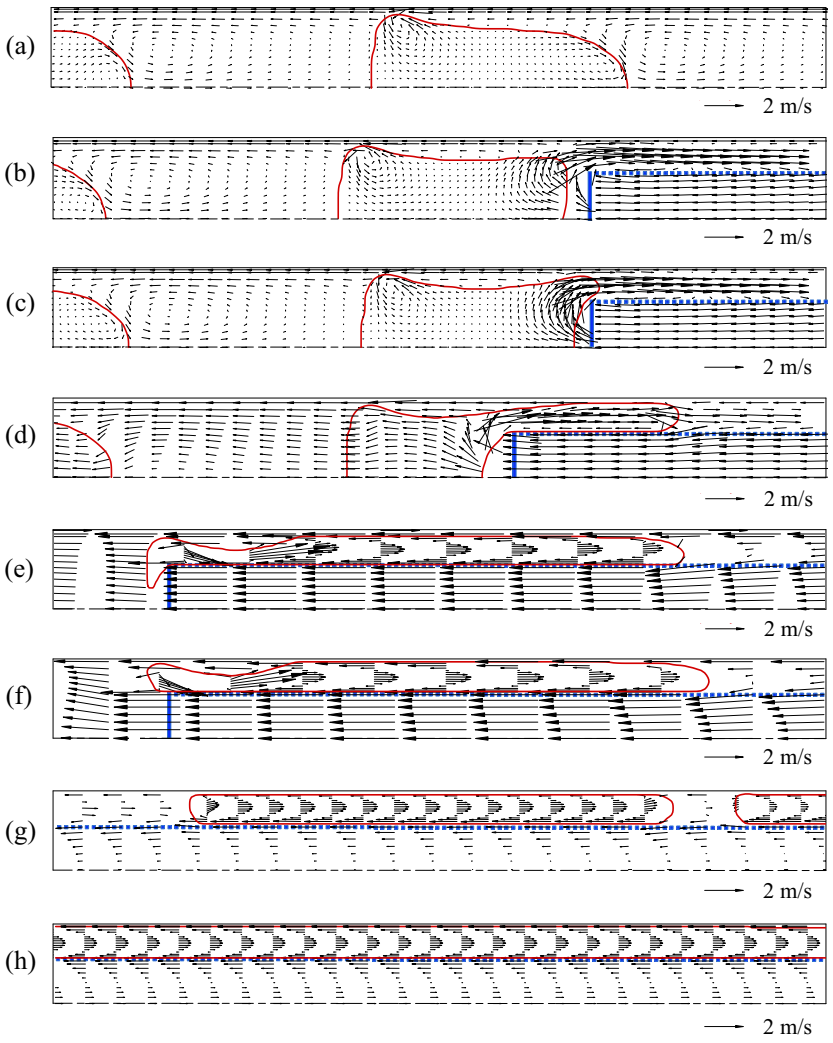

Fig. 6. Velocity field referenced to the attached coordinate on the bubble: (a) t = 14.71 ms, x = 3.9–5.9 mm; (b) t = 16.84 ms, x = 6.6–8.6 mm; (c) t = 16.89 ms, x = 6.6–8.6 mm; (d) t = 17.04 ms, x = 6.8–8.8 mm; (e) t = 18.33 ms, x = 7.7–9.7 mm; (f) t = 17.34 ms, x = 7.7–9.7 mm; (g) t = 18.33 ms, x = 9.9–11.9 mm; (h) t = 21.02 ms, x = 13.4–15.4 mm.

B) and the local area where the bubbles are completely merged (point C). One can find the flow from the side region to the core region at location A. Alternatively, positive radial flow was established at location B, indicating the flow from the core region to the side region. The positive radial flow covers a very short axial flow length. At location C, a clear gas–liquid interface was observed above the pin-fin membrane, under which there was no any mass exchange across the pin-fin membrane.

Fig. 8 shows the radial velocities at t = 13.4 ms, except that the last subfigure shows the merging process at t = 13.6 ms for location D. The two daughter bubbles did not contact each other at t = 13.4 ms, but they are merging at t = 13.6 ms to form the nozzle shape gas–liquid interface. It is observed that positive radial velocities exist at the bubble tail (see the locally enlarged flow field in Fig. 8). The gas–liquid interface is curved at the bubble tail. When the bubble is traveling from left to right, the volume behind the bubble tail should be compensated by liquid from the core region to the side region, forming the positive radial velocities behind the bubble.

5.3. Effect of the two-phase flow rates

This section discussed the effect of flow rates on the separation process. An important parameter characterizing the separation process is the separation length, which was defined as the distance from the separator entrance to the location where bubbles are completely merged. Referring the five runs in Table 1, the flow rate ratios of Q_g/Q_l are varied from 2/6 to 6/6. Fig. 9 shows the quasi-linearly decreased separation lengths when Q_g/Q_l is increased. When the liquid flow rate is fixed, increasing the gas flow rates speeds up the bubble moving velocities in the side region. This effect increased the pressure difference across the pin-fin membrane when the whole duct cross section is occupied by liquid. Therefore, the radial flow rate from the side region to the core region is raised to quickly shorten the liquid plug. For ultra-low flow rate ratio of Q_g/Q_l = 1/6, the bubble train cannot be merged at the duct exit. Thus, the case of Q_g/Q_l = 1/6 was not shown in Fig. 9.

It is noted that the separation lengths were less reported in the literature. At this stage, the direct comparison between the simulation and the measurement is not possible regarding the separation length. The explanation is given here. The increase of Q_g/Q_l indicates the increased gas flow rates and/or decreased liquid flow rates. When the two-phase flow interacts the micro-pin-fin structure, the gas phase enters the side region. It is noted that the bubble lengths were less changed because we assumed a constant bubble volume initially. The increase of gas flow rate means the increase of the bubble formation frequency to shorten the liquid

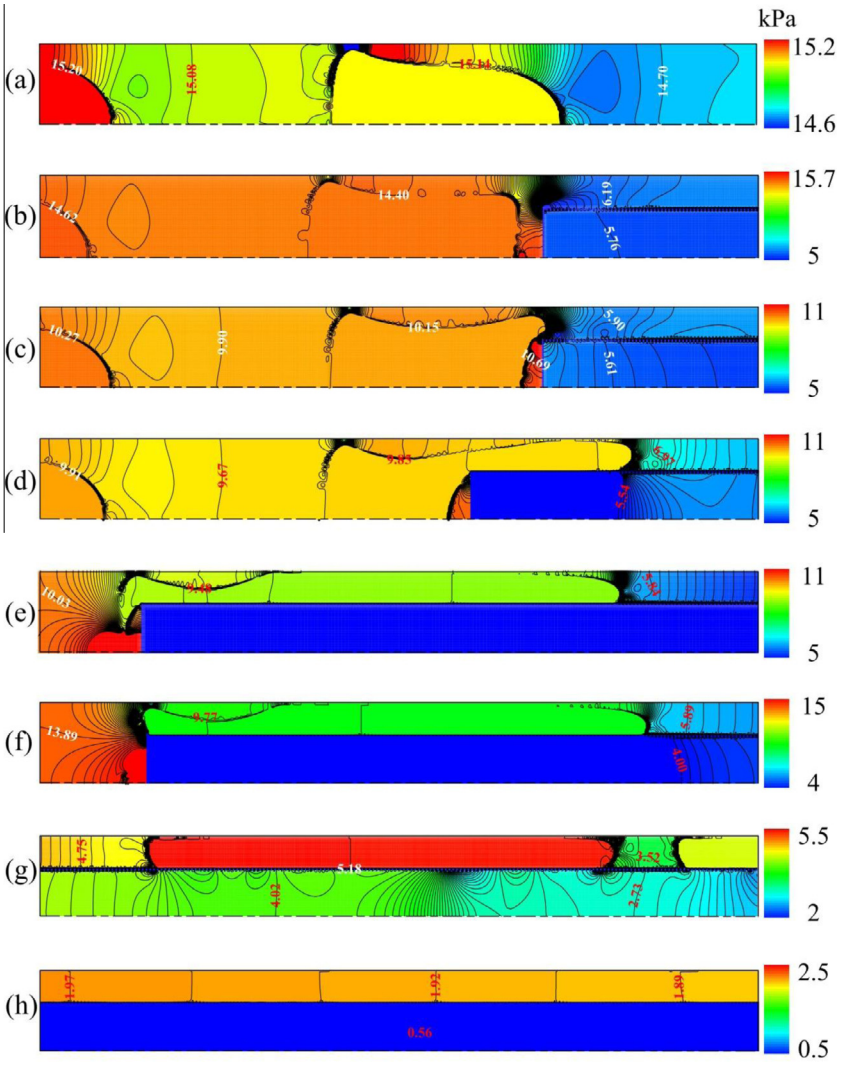

Fig. 7. Pressure field for the basic run: (a) t = 14.71 ms, x = 3.9–5.9 mm; (b) t = 16.84 ms, x = 6.6–8.6 mm; (c) t = 16.89 ms, x = 6.6–8.6 mm; (d) t = 17.04 ms, x = 6.8–8.8 mm; (e) t = 17.32 ms, x = 7.7–9.7 mm; (f) t = 17.34 ms, x = 7.7–9.7 mm; (g) t = 18.33 ms, x = 9.9–11.9 mm; (h) t = 21.02 ms, x = 13.4–15.4 mm (note: pressures are referenced to the environmental pressure).

plug length. Thus, the void fractions are increased to raise the pressure drop in the side region from the micro-separator entrance to the exit. This effect elevates the pressure difference between the side region and the core region, yielding the increased liquid flow rates across the micro-pin-fin membrane to shorten the separation length.

We examined the bubble slug and liquid plug lengths in both the bare duct section and the separator section (see Fig. 10). The two sections are interfaced at x = 8.0 mm (see Fig. 2). In Fig. 10, the red and black symbols represent the bubble slug length and liquid plug length, respectively. Even though the gas flow rates are apparently raised from S-2 to L-2, the bubble slug lengths are weakly changed for different runs. The present simulation gave the correct trend of the slug bubble length in the side region. One shall remember that a constant bubble volume is assumed initially. The increase of the gas flow rates increases the bubble formation frequency. But the slug bubble lengths were less influenced by the gas flow rates due to the constant bubble volume for each bubble. The variations of gas flow rates significantly changed the liquid plug lengths, in both the bare duct section and the separator section. The smaller gas flow rates yielded longer liquid plug lengths, indicating the sparse population of gas bubbles in the duct. On the other hand, the larger gas flow rates involved the dense population of gas bubbles in the duct. Attention was paid to the bubble slug and liquid plug lengths in the bare duct section and the separator section. When a bubble interacts the pin-fin membrane, the bubble was separating into two daughter bubbles, which are significantly elongated in the side region, due to the decreased cross section area in the separator section for the gas phase. The liquid plugs apparently increased the lengths when the liquid plug was approaching the membrane entrance, but the lengths are sharply decreased following the membrane entrance at x = 8.0 mm. The decrease of the liquid plug length caused the bubble coalescence and complete phase separation in the separator section. As observed in Fig. 10, for all the five runs in Table 1, the liquid plug lengths are shortened to about zero at x = 12.0 mm (4.0 mm downstream of the membrane entrance).

Fig. 10 also shows the bubble slug and liquid plug lengths in the bare tube section and the modulated flow section for ultra-low ratio of Q_g/Q_l = 1/6. Bubble slug lengths are not apparently changed by comparing with other flow rate ratio cases, but liquid plug lengths are significantly increased in the bare tube section for Q_g/Q_l = 1/6. The liquid plug length still exists at x = 16 mm, indicating the not complete coalescence of the bubbles in the side region.

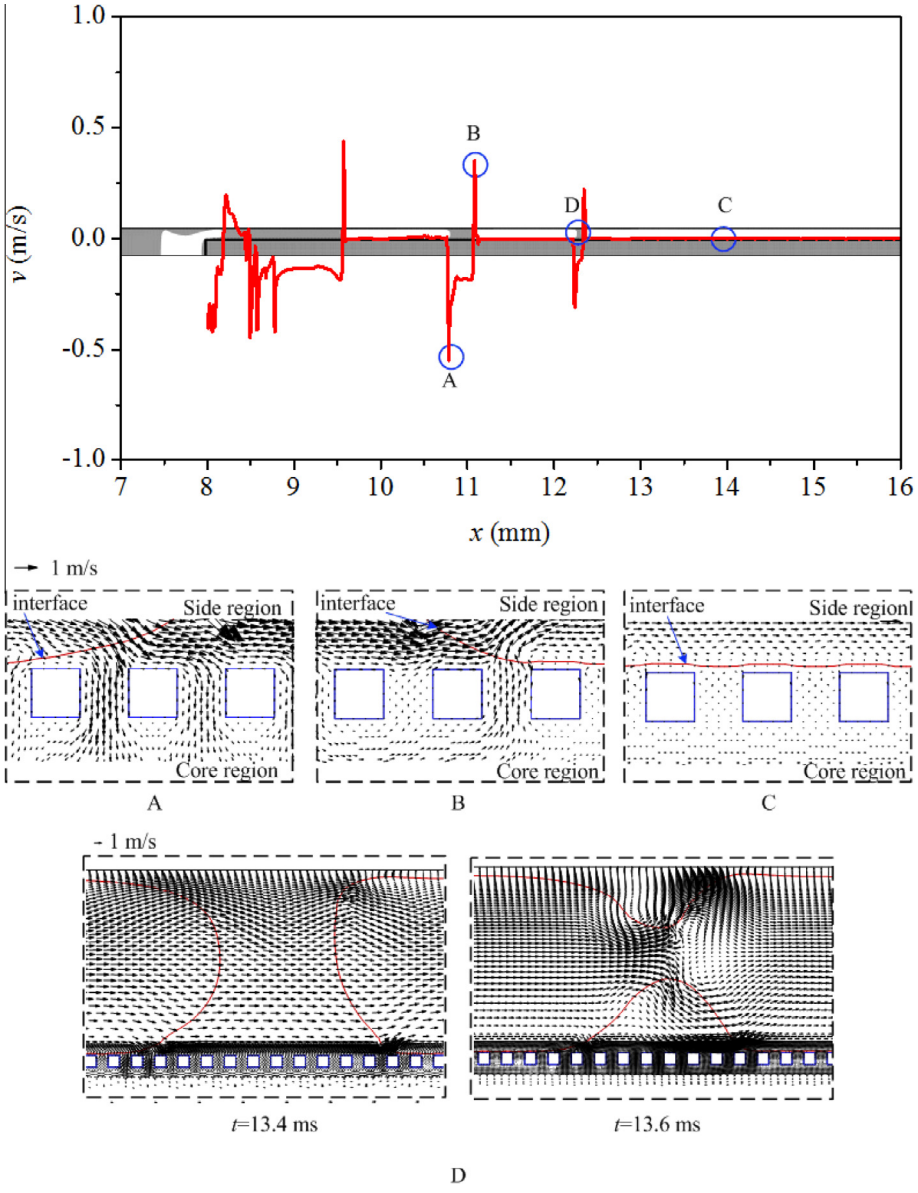

Fig. 8. Radial velocities for the basic run (the results were shown at t = 13.4 ms, the last subfigure shows the enlarged velocity field at t = 13.6 ms).

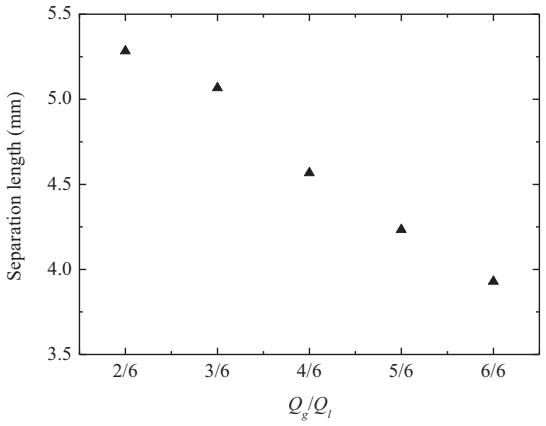

Fig. 9. The separation length versus Q_g/Q_l.

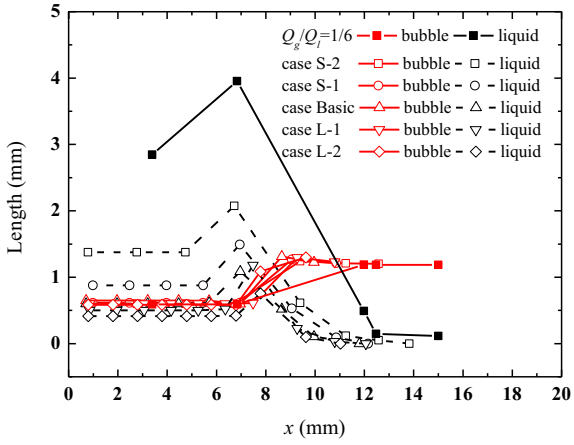

Fig. 10. The lengths of bubble slug and liquid plug along the flow direction. (For interpretation of the references to color in this figure legend, the reader is referred to the web version of this article.)

In order to further examine the effect of flow rates on the separation process, we plotted the referenced velocity fields for S-2 (low gas flow rate) run, basic run and L-2 (large gas flow rate) run in Fig. 11, noting that same focused area was used Fig. 11a and b, but different areas were focused in Fig. 11c and d. It is observed that the L-2 run had shorter liquid plug length for the large gas flow rate. When a bubble was attacking the membrane, strong circulating flow was observed for all the three runs (see Fig. 11a and b). The bubble slug lengths were weakly dependent on the gas flow rates, but the gas flow rates slightly changed the bubble shape, including the liquid film thickness near the duct wall.

We noted that the basic run was set so that the average velocities for the gas phase in the side region and for the liquid phase in the core region were equal. Assuming the "stationary" bubble (referenced coordinate), the gas flow rates strongly changed the liquid flow velocities in the core region. Fig. 11c shows the merging process of two neighboring bubbles, while Fig. 11d shows the complete phase separation with liquid plugs disappearing in the side region. For S-2, Fig. 11c and d shows positive velocities in the core region, indicating the faster traveling velocities of liquid in the core region, due to the smaller flow rate ratio of Q_g/Q_l. For the basic run, negative axial velocities appeared near the pin-fin membrane, but positive velocities appeared near the core region center. The velocity fields were further changed for L-2. The whole core region possessed negative velocities, indicating smaller traveling speed of the liquid phase in the core region.

5.4. Ultra-low and ultra-large gas flow rates

Finally, we talk about the ultra-low and ultra-large gas flow rate runs. If the separator is sufficiently long, the two-phases can be fully separated even at ultra-low gas flow rates. At a specific separator length, the ultra-low gas flow rates may cause the non-complete coalescence of the bubble slugs in the side region. The minimum gas flow rate limit is $Q_g/Q_l = 1/6$ for the present separator design. The ultra-large gas flow rate may cause the bubble breakup and gas leakage towards the core region, leading to the micro-separator failure. Thus, a maximum gas flow rate is specified for a specific separator design.

Fig. 12 shows the referenced pressure distribution during the merging process of two neighboring bubbles in the side region

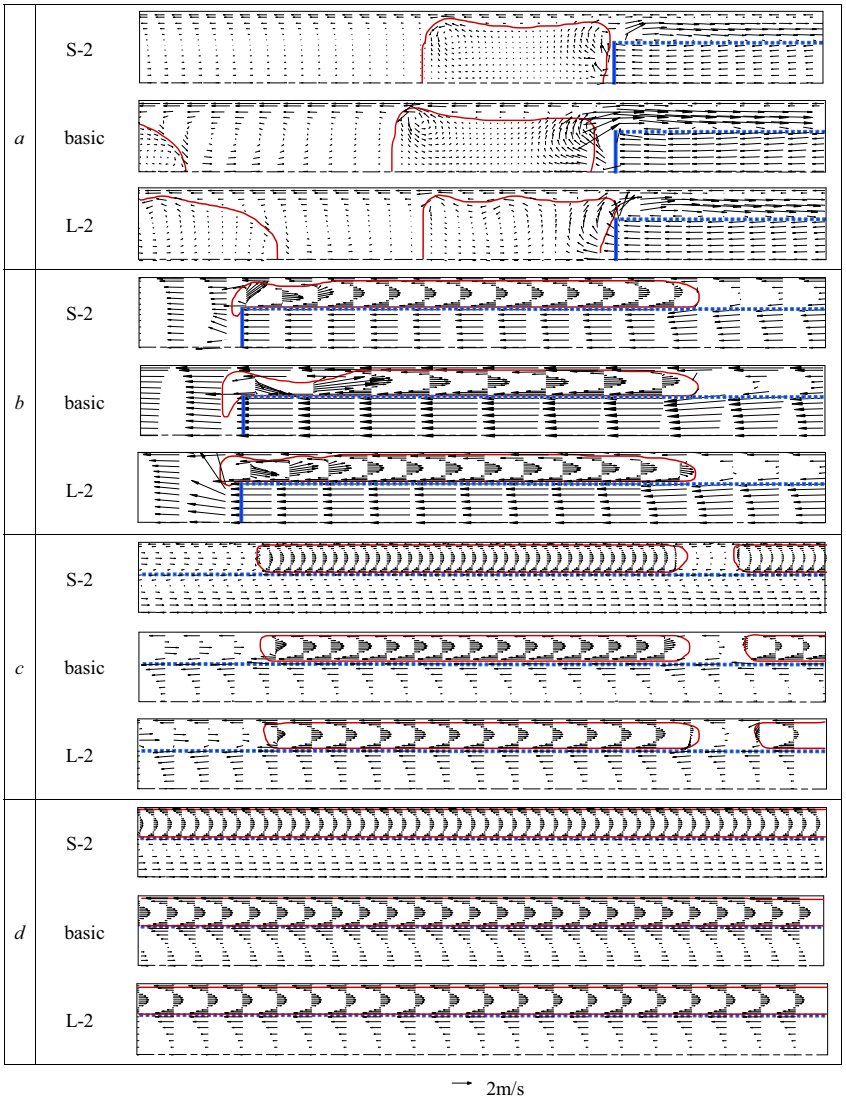

Fig. 11. The referenced velocity field: (a) S-2, t = 19.45 ms; basic, t = 16.84 ms; L-2, t = 15.58 ms; x = 6.6–8.6 mm; (b) S-2, t = 20.01 ms; basic, t = 17.32 ms; L-2, t = 15.93 ms; x = 7.7–9.7 mm; (c) S-2, t = 22.49 ms, x = 4.7–6.7 mm; basic, t = 18.33 ms, x = 9.9–11.9 mm; L-2, t = 16.68 ms, x = 9.7–11.7 mm; (d) S-2, t = 26.85 ms, x = 13.86–15.86 mm; basic, t = 21.02 ms, x = 13.4–15.4 mm; L-2, t = 18.49 ms, x = 13.4–15.4 mm.

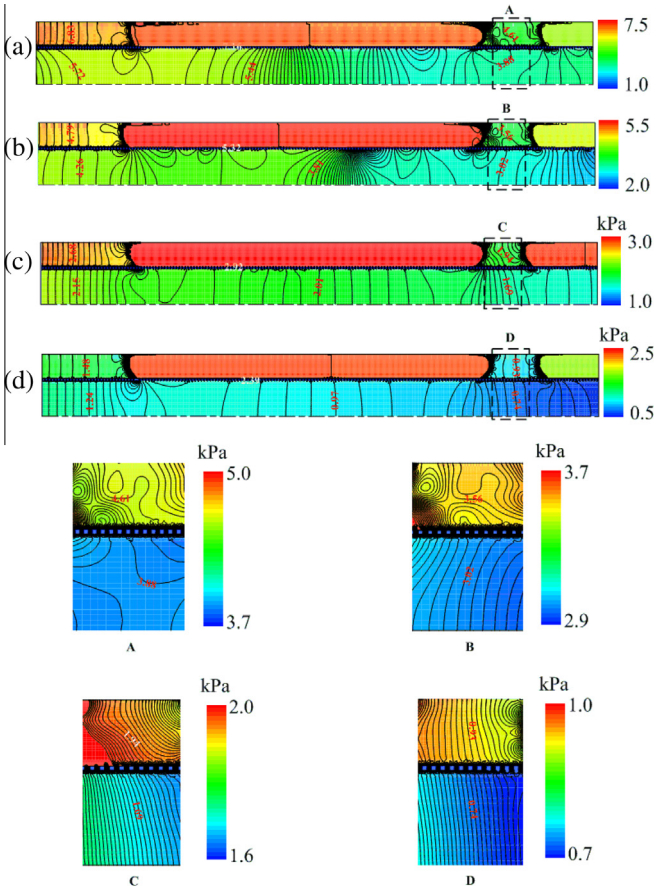

Fig. 12. Pressure field: (a) L-2, t = 16.68 ms, x = 9.7–11.7 mm; (b) basic, t = 18.33 ms, x = 9.9–11.9 mm; (c) S-2, t = 22.49 ms, x = 10.7–12.7 mm; (d) Q_g/Q_l = 1/6, t = 23.37 ms, x = 9.8–11.8 mm.

for L-2 run, basic run, S-2 run and the run for Q_g/Q_l = 1/6. It is easy to understand that pressures inside bubbles are larger than those in liquids around the bubble. We are interested in the pressures when the whole cross section was occupied by liquids. Such locations are marked as A, B, C and D for the four runs, respectively. The local areas were enlarged in Fig. 12. For the small gas flow rate run (S-2), pressures in the side region are larger than those in the core region (see location C). This sustains the pressure driven liquid flow from the side region to the core region, yielding the bubble merging and thus the complete phase separation can take place downstream somewhere. For the ultra-low flow rate case with Q_g/Q_l = 1/6, the pressures are 0.93 kPa in the side region and 0.74 kPa in the core region (see location D in Fig. 12). The pressure difference between the side region and the core region is only 0.19 kPa to drive liquid flow from the side region to the core region. Such pressure difference is so small that the liquid flow rate from the side region to the core region is small, yielding not complete bubble coalescence in the side region, for the modulated flow section of 8.0 mm. The complete bubble coalescence needs longer modulated flow section.

Fig. 13 shows the void fractions in both the bare duct section and the modulated flow section, for the four cases of Q_g/Q_l = 1/6, S-2 run, basic run and L-2 run, respectively. Because the liquid film thicknesses are small compared with the channel cross section size, the void fraction approaches one if the local area is occupied by the gas phase. Alternatively, the void fraction is zero if the local area is occupied by the liquid phase. In fact, the void fraction distribution reflects the gas bubble population density along the flow length. It is seen that the bubbles are densely populated along the flow length when the flow rate ratios of Q_g/Q_l are increased. In the separating section, the bubble population density is increased along the flow length. This paper used the separation length as the characteristic parameter. An alternative parameter is the separation efficiency, which is one for the complete separation cases. The separation efficiency is less than one for the non-complete separation cases such as Q_g/Q_l = 1/6.

Fig. 14 shows that the modulated flow section had a length of L_M. Before the complete merging of bubbles in the side region, the two-phase mixture was flowing in the side region and liquids are flowing in the core region. The exit plane at which the separated phases are discharged out of the separator was called "2", and upstream somewhere was called "1". Regarding the liquid flow in the core region, the pressure drop between locations 1 and 2 is

$$\Delta P_{\text{core}} = P_{1,\text{core}} - P_{2,\text{core}} \tag{19}$$

On the other hand, the two-phase flow in the side region yields the following pressure drop

$$P_{1,\text{side}} - P_{2,\text{side}} = \Delta P_{lo,\text{side}} \varphi_{lo}^2 \tag{20}$$

where $\Delta P_{lo,\text{side}}$ is the frictional pressure drop assuming the whole two-phase flow rate flowing as liquid only and φ_{lo}^2 is the two-phase multiplier. The pressure difference across the pin-fin membrane at the plane 1 is

$$P_{1,\text{side}} - P_{1,\text{core}} = \Delta P_{lo,\text{side}} \varphi_{lo}^2 - \Delta P_{\text{core}} + P_{2,\text{side}} - P_{2,\text{core}} \tag{21}$$

Due to the fact that $P_{2,\text{side}} = P_{2,\text{core}}$ at the exit plane 2, Eq. (21) is rewritten as

$$P_{1,\text{side}} - P_{1,\text{core}} = \Delta P_{lo,\text{side}} \varphi_{lo}^2 - \Delta P_{\text{core}} \tag{22}$$

Based on the two-phase flow theory [38], the two-phase flow multiplier φ_{lo}^2 has large values ranging from 10 to 100, Eq. (22) is larger than zero, maintaining the driving force for liquid flow across the pin-fin membrane. The redial velocity V_r across the micro-pin-fin membrane for a single pore is

$$\Delta P_{lo,\text{side}} \varphi_{lo}^2 - \Delta P_{\text{core}} = C_d \frac{\rho_l V_r^2}{2} \tag{23}$$

where C_d is the discharge coefficient for a fluid stream flowing through a nozzle just like the pore in this study. For the complete separation of the two-phases, one shall remember that the total liquid flow rate flows from the side region to the core region. The following equation exists:

$$Q_l = V_r n_l A_{pore} \tag{24}$$

Where n_l is the number of pores that are occupied by liquids in both the side region and the core region, A_{pore} is the pore area for the liquid flowing through. The separation length for the complete two-phase separation is

$$L_s = (n_l + n_g)(w + d) \tag{25}$$

where n_g is the number of pores that are occupied by gas in the side region, $w + d$ is the length for a single rectangular pore. The value of n_l is determined by Eqs. (23) and (24). The ratio of n_g/n_l is related to the average void fraction in the side region of the separator.

The separator works based on the capillary principle. It should be assured that the pressures inside the bubble are smaller than the capillary pressure generated by the small holes of the neighboring pin-fins. When the gas flow rate was increased to the value given for L-2 run, the pressure criterion is not satisfied. The bubble breakup takes place. Fig. 15 tracks the bubble shape and flow field at t = 4.05 ms and 4.08 ms. The bubble breakup did not happen at t = 4.05 ms but it did happen at t = 4.08 ms. When the bubble is attacking the pin-fin membrane, an enclosed and complete gas–liquid interface is maintained at t = 4.05 ms. This time is called

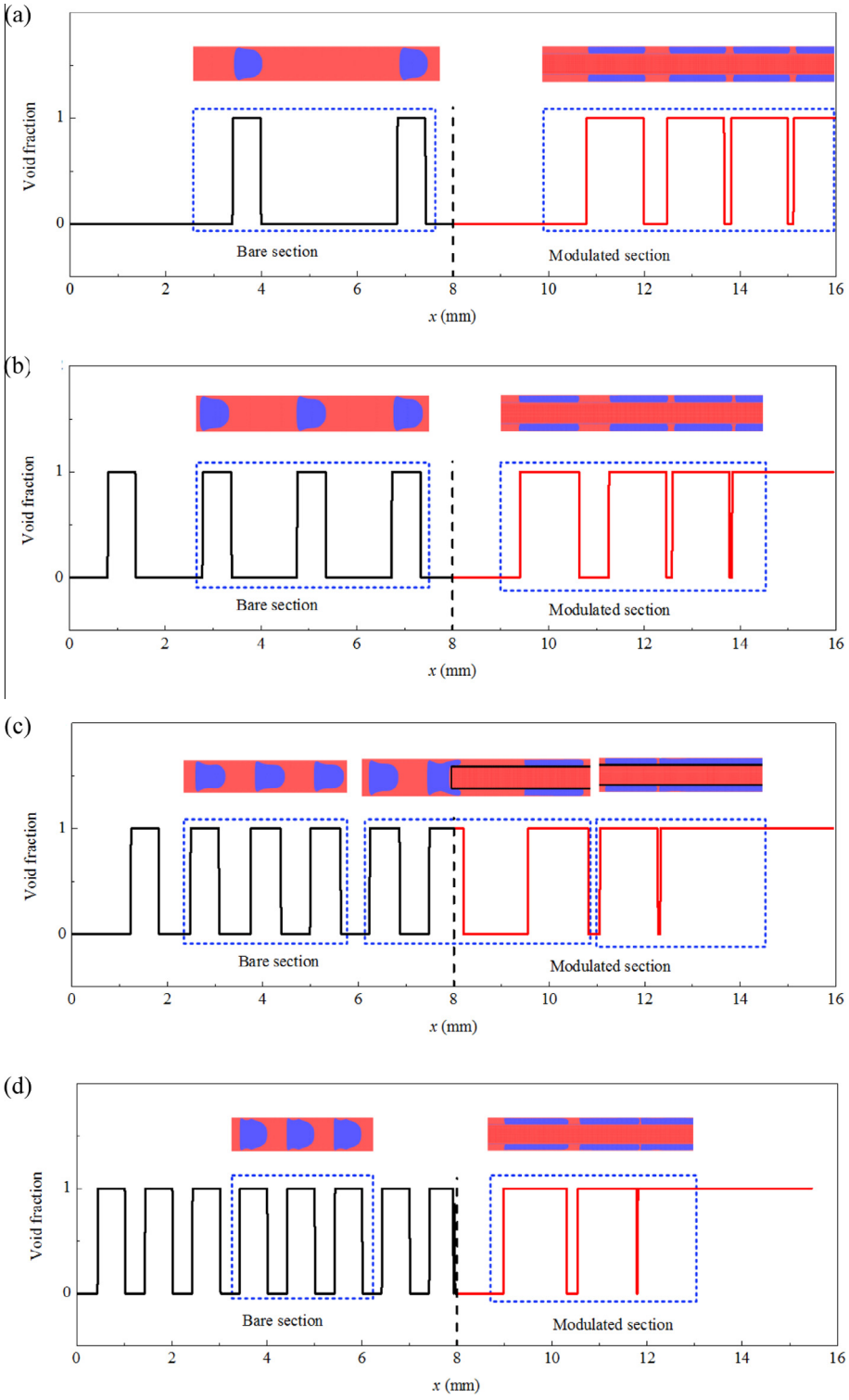

Fig. 13. The volume fraction along the bare tube section and the side region of the modulated flow section (a) $Q_g/Q_l = 1/6$, $t = 29.07$ ms; (b) S-2, $t = 21.84$ ms; (c) basic, $t = 15.99$ ms; (d) L-2, $t = 13.29$ ms.

the normal bubble separating time, on which two daughter bubbles are being separated from its mother bubble. However, the ultra-large gas flow rate yields large pressures inside the bubble to exceed the capillary pressure limit that can be provided by the interface curvature within the membrane holes. Thus, the bubble breakup happens on the second membrane hole at $t = 4.08$ ms. The gas–liquid interface is not complete and the gas phase sharply discharges into the core region, involving large discharge velocities

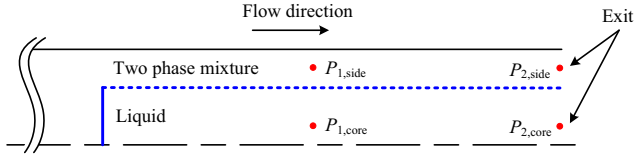

Fig. 14. The drawing to show why the separator can work at ultra-low gas flow rates.

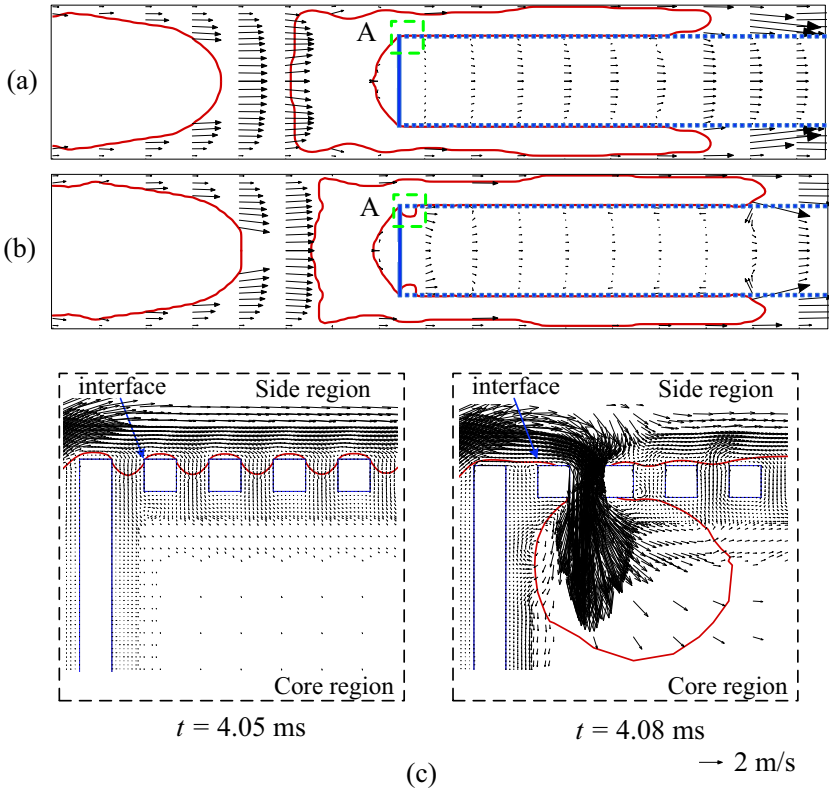

Fig. 15. Bubble shape and velocity field for the maximum gas flow rate run (see Table 1).

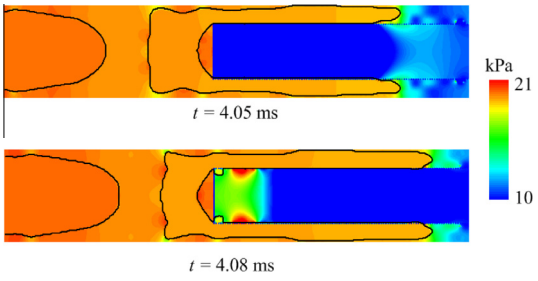

Fig. 16. The pressure distribution during the bubble breakup process for the maximum gas flow rate run.

in the core region. Fig. 16 shows the referenced pressures at $t = 4.05$ ms and 4.08 ms. Pressures inside the core region is small at $t = 4.05$ ms. After a short time elapsed at $t = 4.08$ ms, pressures in the core region upstream are sharply raised. Because the capillary pressure is inversely proportional to the hole size (d), the decrease of d increases the capillary pressure to extend the gas flow rate operation range.

6. Conclusions

The following conclusions can be drawn

- A micro-pin-fin membrane separator was proposed using capillary separation principle. An enclosed membrane with micron scale holes was symmetrically populated in a rectangular duct. When gas phase interacts the membrane, the gas–liquid interface cannot penetrate the pin-fin holes due to the increased surface energy.
- A two-dimensional numerical model simulated the separation process with multiscale feature. The VOF method tracked the gas–liquid interface. Multiscale grids adapted the near wall region and pin-fin region.
- When a bubble attacks the pin-fin membrane, strong liquid circulation occurs at the membrane entrance. Pressures inside the bubble are larger than those in liquids. Pressures in the side region are larger than those in the core region. Liquid plugs are gradually shortened due to the pressure driven flow from the side region to the core region to cause the bubble coalescence.
- The increase of gas flow rates shortened the separation length. The gas flow rates did not apparently change the bubble length. Large gas flow rates yield densely populated gas bubbles in the duct. The liquid plug lengths are quickly shortened following the membrane entrance.
- The frictional pressure drop of the two-phase mixture in the side region was larger than that of liquids in the core region, which is the major reason for the separator to work at low or normal two-phase flow rates. The ultra-large gas flow rates yielded quite large bubble pressures to exceed the capillary pressure limit generated by pin-fin holes, causing the separator failure. The decrease of the pin-fin hole size increased the capillary pressure limit.

Acknowledgements

This paper was supported by the National Natural Science Foundation of China (51436004) and the International Cooperation Project of NSFC (51210011).

References

[1] P.A. Auroux, D. Iossifids, D.R. Reyes, A. Manz, Micro total analysis systems. 1. Analytical standard operations and applications, Anal. Chem. 74 (2002) 2637.
[2] D.R. Reyes, D. Iossifids, P.A. Auroux, A. Manz, Micro total analysis systems. 1. Introduction, theory, and technology, Anal. Chem. 74 (2002) 2623.
[3] V. Hessel, A. Renken, J.C. Schouten, J. Yoshida, Micro Process Engineering: A Comprehensive Handbook—Fundamentals, Operation and Catalysts, Wiley VCH, Weinheim, 2009.
[4] C.X. Zhao, A.P.J. Middelberg, Two-phase microfluidic flows, Chem. Eng. Sci. 66 (2011) 1394–1411.
[5] G.P. Willems, B.P. van Esch, J.J.H. Brouwers, M. Golombok, Creeping film model for condensed centrifugal separation processes, Chem. Eng. Sci. 63 (2008) 3358–3365.
[6] Q. Ma, D. Hu, G. He, S. Hu, W. Liu, Q. Xu, Y. Wang, Performance of inner-core supersonic gas separation device with droplet enlargement method, Chin. J. Chem. Eng. 17 (6) (2009) 925–933.
[7] B.J. Azzopardi, Phase separation at T-junctions, Multiphase Sci. Technol. 11 (1999) 223–329.
[8] A. Azzi, A. Al-Attiyah, L. Qi, W. Cheema, B.J. Azzopardi, Gas–liquid twophase flow division at a micro-T-junction, Chem. Eng. Sci. 65 (2010) 3986–3993.
[9] G. Das, P.K. Das, B.J. Azzopardi, The split of stratified gas–liquid flow at a small diameter T-junction, Int. J. Multiphase Flow 31 (2005) 514–528.
[10] K. He, S. Wang, J. Huang, The effect of flow pattern on split of two-phase flow through a micro-T-junction, Int. J. Heat Mass Transfer 54 (2011) 3587–3593.
[11] C. Adiche, K. Sundmacher, Experimental investigation on a membrane distillation based micro-separator, Chem. Eng. Process. 49 (2010) 425–434.
[12] M.P. David, J. Miler, J.E. Steinbrenner, Y. Yang, M. Touzelbaev, K.E. Goodson, Hydraulic and thermal characteristics of a vapor venting two-phase microchannel heat exchanger, Int. J. Heat Mass Transfer 54 (2011) 5504–5516.
[13] M. Kraus, U. Krewer, Experimental analysis of the separation efficiency of an orientation independent gas/liquid membrane separator, Sep. Purif. Technol. 81 (2011) 347–356.
[14] S.B. Saad, P. Clement, C. Gentric, J.-F. Fourmigue, J.-P. Leclerc, Experimental distribution of phases and pressure drop in a two-phase offset strip fin type compact heat exchanger, Int. J. Multiphase Flow 37 (2011) 576–584.
[15] F. Zenith, M. Kraus, U. Krewer, Model-based analysis of micro-separators for portable direct methanol fuel-cell systems, Comput. Chem. Eng. 38 (2012) 64–73.
[16] L.E. Wiesegger, R.P. Knauss, G.E. Guntschnig, J.J. Brandner, R.J. Marr, Vapor–liquid phase separation in micro-/ministructured devices, Chem. Eng. Sci. 93 (2013) 32–46.
[17] R. Gupta, D.F. Fletcher, B.S. Haynes, On the CFD modelling of Taylor flow in microchannels, Chem. Eng. Sci. 64 (2009) 2941–2950.
[18] A. Günther, K.F. Jensen, Multiphase microfluidics: from flow characteristics to chemical and materials synthesis, Lab Chip 6 (2006) 1487–1503.
[19] A. Günther, S.A. Khan, M. Thalmann, F. Trachsel, M.A. Schmidt, K.F. Jensen, Transport and reaction in microscale segmented gas–liquid flow, Lab Chip 4 (2004) 246–278.
[20] A. Günther, M. Jhunjhunwala, M. Thalmann, M.A. Schmidt, K.F. Jensen, Micromixing of miscible liquids in segmented gas–liquid flow, Langmuir 21 (2005) 1547–1555.
[21] M.D. Roydhouse, M. Pradas, N. Al-Rifai, B. Azizi, E. Cao, S. Kalliadasis, A. Gavriilidis, Operating ranges of gas–liquid capillary microseparators: experiments and theory, Chem. Eng. Sci. 114 (2015) 30–39.
[22] A. Aota, M. Nonaka, A. Hibara, T. Kitamori, Countercurrent laminar microflow for highly efficient solvent extraction, Angew. Chem. Int. Ed. 46 (2007) 878.
[23] B. Zhao, J.S. Moore, D.J. Beebe, Surface-directed liquid flow inside microchannels, Science 291 (2001) 1023.
[24] C.C. Hsieh, S.C. Yao, Development of a microscale passive gas–liquid separation system, in: Proceedings of the 5th International Conference on Multiphase Flow, Yokohama, Japan, 2004.
[25] A. Hibara, S. Iwayama, S. Matsuoka, M. Ueno, Y. Kikutani, M. Tokeshi, T. Kitamori, Surface modification method of microchannels for gas–liquid two phase flows in microchips, Anal. Chem. 77 (2005) 943–947.
[26] F. Zenith, M. Kraus, U. Krewer, Model-based analysis of micro-separators for portable direct methanol fuel-cell systems, Comput. Chem. Eng. 38 (2012) 64–73.
[27] J.L. Xu, B. An, D.L. Sun, The phase separation in a rectangular microchannel by micro-membrane, Appl. Therm. Eng. 88 (2014) 172–184.
[28] R.C. Cammarata, Surface and interface stress effects in thin films, Prog. Surf. Sci. 46 (1994) 1–38.
[29] D.Y. Qian, A. Lawal, Numerical study on gas and liquid slugs for Taylor flow in a T-junction microchannel, Chem. Eng. Sci. 61 (2006) 7609–7625.
[30] C.W. Hirt, B.D. Nichols, Volume of fluid (VOF) method for the dynamics of free boundaries, J. Comput. Phys. 39 (1981) 201–225.
[31] F.P. Bretherton, The motion of long bubbles in tubes, J. Fluid Mech. 10 (1961) 166–188.
[32] J.U. Brackbill, D.B. Kothe, C. Zemach, A continuum method for modeling surface tension, J. Comput. Phys. 100 (1992) 335–354.
[33] A. Mehdizadeh, S.A. Sherif, W.E. Lear, Numerical simulation of thermofluid characteristics of two-phase flow in microchannels, Int. J. Heat Mass Transfer 54 (2011) 3457–3465.
[34] G.I. Taylor, Deposition of a viscous fluid on the wall of a tube, J. Fluid Mech. 10 (1960) 161–165.
[35] P. Aussillous, D. Quere, Quick deposition of a fluid on the wall of a tube, Phys. Fluids 12 (2000) 2367–2371.
[36] M. Kreutzer, F. Kapteijn, J.A. Moulijn, Inertial and interfacial effects on pressure drop of Taylor flow in capillaries, AIChE J. 51 (9) (2005) 2427–2440.
[37] T. Taha, Z.F. Cui, CFD modeling of slug flow inside square capillaries, Chem. Eng. Sci. 61 (2006) 665–675.
[38] C. Kleinstreuer, Two-Phase Flow: Theory and Applications, CRC Press, 2003.